Joule

Article

Enhancing the viability of p-i-n perovskite solar cells with printable carbon cathode: Origin of polarity inversion

Graphical abstract

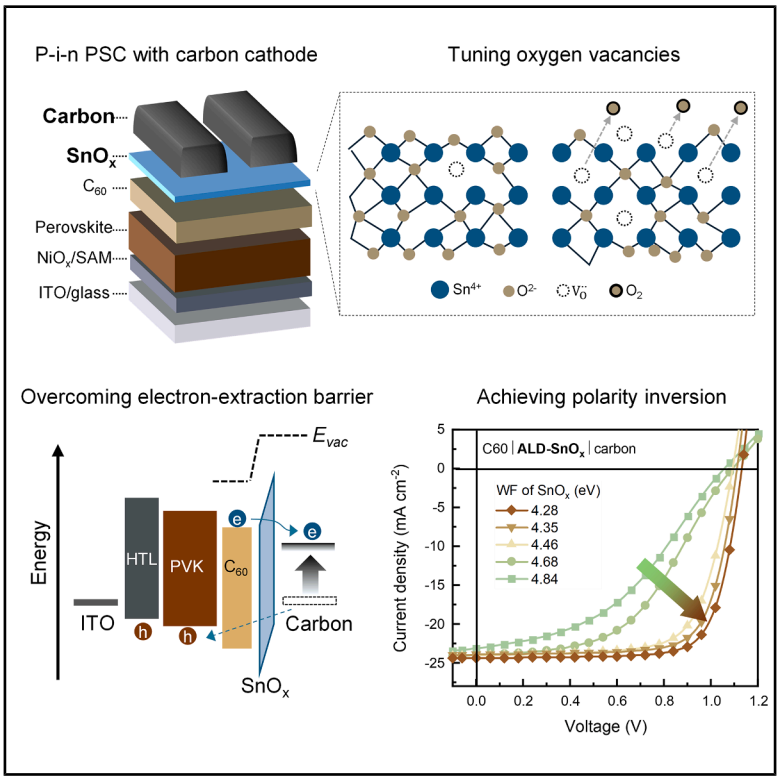

Highlights

- Employs printable carbon as the cathode of p-i-n perovskite solar cells
- Enables polarity inversion of carbon with a tin oxide interlayer
- Comparable PCE, improved longevity, and lower material cost, compared with Ag electrode
- Provides a generalized contact design rule for metal-free PSCs

Authors

Tian Du, Hakan U. Dag, Zijian Peng, ..., Olga Kasian, Julien Bachmann, Christoph J. Brabec

Correspondence

tian.du@fau.de (T.D.), christoph.brabec@fau.de (C.J.B.)

In brief

Carbon is an abundant, printable, and chemically stable electrode material, but until now, it could not be used as the cathode in p-i-n perovskite solar cells. We overcome this long-standing limitation by introducing a mechanically robust and electronically tuned tin oxide interlayer that inverses carbon's polarity and enables efficient electron extraction. This advances metal-free device design, delivers high efficiency, and provides remarkably longer operational lifetimes and major cost reductions, boosting the industrial viability of perovskite photovoltaics.

Du et al., 2026, Joule *10*, 102224
January 21, 2026
https://doi.org/10.1016/j.joule.2025.102224

CellPress

Joule

CellPress
OPEN ACCESS

Article

Enhancing the viability of p-i-n perovskite solar cells with printable carbon cathode: Origin of polarity inversion

Tian Du,[1,2,6,*] Hakan U. Dag,[1,2,6] Zijian Peng,[2] Jonas Englhard,[3] Anastasia Barabash,[2] Handan Zhang,[2] Jiyun Zhang,[1,2] Jiayi Tan,[1,2] Shudi Qiu,[2] Lirong Dong,[2] Michael Wagner,[1] Jens A. Hauch,[1] Fei Guo,[4] Olga Kasian,[1,2,5] Julien Bachmann,[3] and Christoph J. Brabec[1,2,7,*]

[1]Forschungszentrum Jülich GmbH, Helmholtz-Institute Erlangen-Nürnberg (HI ERN), Immerwahrstraße 2, 91058 Erlangen, Germany
[2]Department of Material Science, Materials for Electronics and Energy Technology (i-MEET), Friedrich-Alexander-Universität Erlangen-Nürnberg, Martensstraße 7, 91058 Erlangen, Germany
[3]Department of Chemistry and Pharmacy, Section Materials Chemistry, Chemistry of Thin Film Materials, Friedrich-Alexander-Universität Erlangen-Nürnberg, IZNF, Cauerstraße 3, 91058 Erlangen, Germany
[4]Institute of New Energy Technology, College of Physics and Optoelectronic Engineering, Jinan University, Guangzhou 510632, China
[5]Helmholtz-Zentrum Berlin GmbH, Hahn-Meitner-Platz 1, 14109 Berlin, Germany
[6]These authors contributed equally
[7]Lead contact
*Correspondence: tian.du@fau.de (T.D.), christoph.brabec@fau.de (C.J.B.)
https://doi.org/10.1016/j.joule.2025.102224

CONTEXT & SCALE Perovskite solar cell is an emerging photovoltaic technology that is potentially easy to manufacture at large scale. However, bringing these devices from the lab to industrial production may require every layer, especially the rear electrode, to be fabricated using low-cost, high-throughput printing methods. To date, most high-efficiency devices rely on expensive metal electrodes such as silver, which increases costs and reduces the device's long-term stability. Carbon is an abundant, printable, and chemically stable alternative and has been successfully used in one common device layout, the "n-i-p" (so-called "conventional") perovskite architecture. Yet, in the p-i-n (so-called "inverted") architecture, carbon has fundamentally been incompatible because it collects the wrong type of electrical charge.

This work resolves this long-standing incompatibility. We demonstrate that carbon can be used as the electron-collecting electrode in inverted perovskite solar cells by introducing a tailored ultra-thin tin oxide interlayer. This interlayer is both mechanically strong to survive printing and electronically tuned to overcome the inherent energy barrier that previously prevented electrons from flowing into carbon. By understanding and controlling how atomic-level defects in tin oxide influence charge transfer, we convert carbon from a hole-collecting material into an efficient electron collector.

The result is a carbon-based device with comparable performance, remarkably longer operational lifetime, and over 60% lower material cost, compared with its silver-based counterparts. Our findings establish a general physical principle for designing interfaces between n-type metal oxides and carbon for electron extraction, opening a new pathway toward metal-free, scalable, and durable perovskite solar cells. In doing so, we address one of the last major obstacles to fully printed, low-cost solar manufacturing at industrial scale.

SUMMARY

Printable rear electrodes represent a key enabling technology for the upscaling of perovskite solar cells (PSCs). Carbon electrodes are appealing candidates widely employed in n-i-p (so-called "conventional") architectures, but their integration into p-i-n (so-called "inverted") architectures is prohibited by interfacial energetic mismatch. We address this challenge by introducing a tin oxide (SnO_x) interlayer with desirable mechanical durability and n-doping level. We show in detail how the tailored interlayer converts carbon from a hole-collecting anode to an electron-collecting cathode and how the electron-extraction barrier is minimized, narrowing the efficiency gap between carbon (21.8%) and silver (24.0%) electrodes. The advancement results in a remarkably improved viability of the PSCs: a modest drop in efficiency is

outweighed by a 3-fold improvement in projected operational lifetime (>8,000 h) and a 60% reduction in the bill of materials. These results underscore the potential of carbon as a cost-effective alternative to silver in the industrialization of p-i-n PSCs.

INTRODUCTION

Metal-halide perovskite solar cells (PSCs) have surged to the forefront of photovoltaic (PV) research, propelled by their exceptional power conversion efficiencies (PCEs) and the promise of high-throughput, roll-to-roll manufacturing.[1] While considerable progress has been made in printing perovskite films[2,3] and charge transport layers,[4] the fabrication of the rear electrodes remains a bottleneck hindering upscaling.[5,6] Vacuum-deposited metal electrodes increase capital and operating costs and constrain throughput. By contrast, carbon recently emerged as a viable alternative for the rear electrode owing to material abundance,[7] ease of upscaling in ambient conditions,[3] and compatibility with printing techniques.[8]

Most carbon-electrode demonstrations to date employ the n-i-p (so-called "conventional") architecture, achieving PCEs > 22% at the cell level and >16% in mini-modules.[3,9,10] In this architecture, carbon serves either as the anode atop a hole transport layer (HTL)[11] or as a combined hole transport/collector in HTL-free stacks.[12] However, carbon's high work function (WF) and partial hole selectivity[13] has largely prohibited its use as cathode in p-i-n (so-called "inverted") devices, leaving few reports, despite the rapid efficiency gains and commercialization momentum of p-i-n PSCs.[14,15] This study targets this deficiency by enabling high-performance carbon electrodes in the p-i-n PSC.

In p-i-n PSCs, photo-generated electrons are extracted through a fullerene-based electron transport layer (ETL) to the cathode. Because ETL/cathode energy levels are often misaligned, an interlayer is required to suppress extraction barriers and enable efficient electron collection.[16] With carbon cathode, conventional interfacial materials—such as bathocuproine (BCP), lithium fluoride (LiF), and metal oxides[17]—may fail to adequately mitigate this misalignment. Printing carbon from wet pastes further complicates interfaces by introducing mechanical and chemical stress that is not seen with physical-vapor-deposited metals.[18–20] Therefore, a tailored interlayer that is both mechanically robust under printing and electronically tunable is needed to render an anode-to-cathode polarity inversion for carbon.

Our work therefore leverages atomic layer deposition (ALD) to create a uniform but non-stoichiometric tin oxide (SnO_x) interlayer.[21] This approach simultaneously achieves two critical objectives: (1) forming a mechanically robust film that withstands subsequent electrode printing from wet paste and (2) tuning oxygen vacancies to mitigate electron extraction losses at the SnO_x/carbon Schottky barrier. These advances enable successful integration of carbon electrode into p-i-n PSCs, yielding device performance among the highest reported values of carbon-electrode PSCs. While substituting silver with carbon results in a small reduction in PCE, this trade-off is outweighed by extension of device longevity and reduction of material cost, underscoring a viable pathway toward durable, low-cost, and scalable perovskite PVs.

RESULTS

Polarity inversion of carbon with a robust ALD-SnO_x interlayer

The purpose of our study, illustrated in Figure 1A, is to employ printable carbon as the rear electrode of the so-called "p type-intrinsic-n type (p-i-n)," also referred to as "inverted," PSCs. Our device employs indium-doped tin oxide (ITO)-coated glass as substrate; nickel oxide (NiO_x) with a self-assembled monolayer (SAM), which is (4-(3,6-dimethyl-9H-carbazol-9-yl)butyl)-phosphonic acid (Me-4PACz), as HTL; and buckminsterfullerene (C_{60}) as ETL. As revealed by Figure 1B, carbon has a higher WF (4.82 eV) than gold (4.77 eV) and silver (4.53 eV) and exhibits partial hole selectivity, and it was therefore used as an anode in n-i-p PSCs.[22] The key challenge of this study, depicted in Figure 1C, is to invert the polarity of carbon from a hole-collecting anode to an electron-collecting cathode.

Figures 1D–1G plot the representative current density-voltage (JV) curves of different electrode-interlayer couples, showing that an SnO_x interlayer through ALD (see Figure S1) is uniquely effective at enabling a printed carbon electrode to operate as a cathode; without an interlayer, Figure 1D, the device with Ag exhibits a rectified JV curve but low fill factor (FF) and open-circuit voltage (V_{OC}), whereas Au and carbon devices show non-rectifying characteristics. Conventional interlayers, such as BCP (Figure 1E) or SnO_x nanoparticles (Figure 1F), recover electron selectivity for Ag/Au but not for carbon. By contrast, after optimization of the reaction temperatures (see Figure S2), ALD-SnO_x restores strong JV rectification for carbon and elevates device performance toward the Ag/Au baselines, Figure 1F.

The above observations suggest a generic energy offset between C_{60} and Ag, Au or carbon, and the need of an interlayer to reduce such offset to enable a working solar cell. For printed carbon, the decisive factor is interlayer integrity under printing. When this is maintained by ALD, energetic tuning becomes effective, and polarity inversion of carbon is realized. The coating of carbon paste appears to completely "wash away" BCP and considerably permeates SnO_x nanoparticle, resulting in a negligible energy-tuning effect. On the contrary, ALD ensures sufficient layer integrity against the ingress of carbon paste and eventually forms a conformal SnO_x/carbon bilayer.

To demonstrate the importance of layer integrity and that a minimum thickness is required to achieve this, we examined the dependence of device performance on the thickness of ALD-SnO_x, which is systematically tuned by controlling the growth rate and cycle numbers of ALD (see Figures S3–S6). Surface scanning electron microscopic (SEM) images, Figures 2A–2D, show increasing continuity of SnO_x on C_{60} with the increase of its thickness. Accordingly, the JV curves of the carbon devices, Figure 2E, show noticeable drops of V_{OC} and FF as

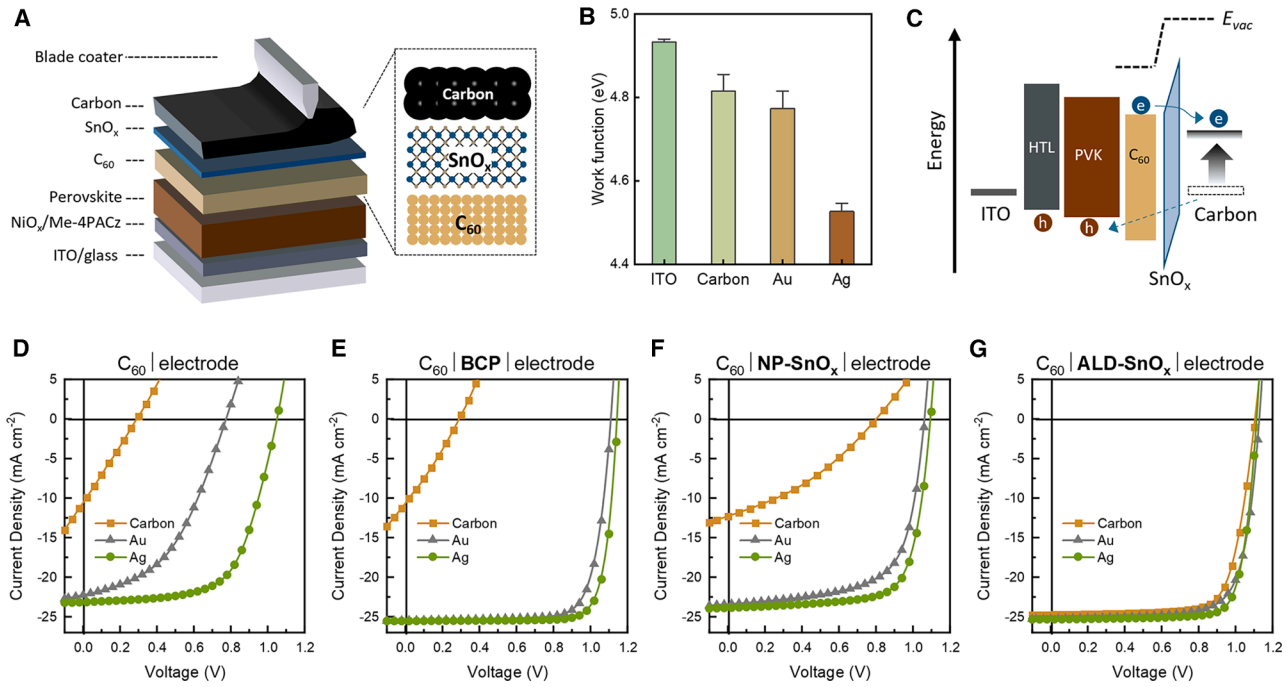

Figure 1. Electrode and interlayer engineering for p-i-n PSC

(A) Schematic drawing of the layer configuration of a p-i-n PSC with printed carbon electrode.

(B) The WF of an ITO substrate, an evaporated gold (Au) electrode, an evaporated silver (Ag) electrode, and a printed carbon electrode (thickness is 20 μm), all measured with a Kelvin probe.

(C) Schematic drawing of the energy diagram of perovskite (PVK)/C_{60}/carbon interface with an energy-level-tuning interlayer.

(D–G) Representative JV curves of inverted PSCs employing Au, Ag, and carbon electrodes without interlayer (D), with BCP (E), SnO_x nanoparticles (F), and ALD-SnO_x (G) as the interlayer.

SnO_x thickness is reduced, resulting in a decrease of average PCE from 19.3% ± 1.4% (25 nm) to 12.6% ± 0.5% (5 nm). In comparison, Ag devices exhibit only minor performance drift, Figure 2F (see Figure S7 for statistical data), from 21.7% ± 0.5% (20 nm) to 19.2% ± 0.4% (5 nm). These results suggest that a minimum thickness is needed for ALD-SnO_x to form a continuous barrier, which prevents ingress by carbon paste and establishes an intended SnO_x/carbon interface. Below this threshold, carbon ingresses through pinholes or weak regions and makes undesired local C_{60}/carbon contacts, resulting in partial loss of electron selectivity and thereby strong surface recombination. In this regard, in Figure 2G, a cross-sectional SEM image is shown highlighting the formation of a well-defined, conformal SnO_x/carbon bilayer with a SnO_x thickness of approximate 25 nm.

Tuning SnO_x's WF for enhanced electron extraction to carbon

With SnO_x's integrity confirmed as essential to maintaining electron selectivity, we now optimize device performance by tuning the WF of SnO_x. As illustrated in Figure 3A, the as-deposited SnO_x films, which are typically amorphous when prepared from ALD,[21] are subjected to thermal annealing or ultraviolet (UV) irradiation treatments.[23] They are reported to stimulate the formation of oxygen vacancies ($V_O^{\cdot\cdot}$) within bulk SnO_2 when performed in a nitrogen (N_2) environment but annihilate $V_O^{\cdot\cdot}$ or creates oxygen interstitials (O_i'') when carried out in ambient air—a process referred to as self-doping[24] and described with the well-known defect reaction written in Kröger-Vink notation as follows:

$$O_O \leftrightharpoons \frac{1}{2}O_2\uparrow + V_O^{\cdot\cdot} + 2e, \qquad \text{(Equation 1)}$$

These treatments were optimized iteratively by monitoring the WF shift of SnO_x as quality control (QC) metric measured with a Kelvin probe. In Figure 3B, we show a progressive change of WF from 4.29 to 4.84 eV by varying the processing parameters. The change of WF is found partially reversible (Figure S8), consistent with and supporting our hypothesis that change of WF is caused by self-doping in which formation of $V_O^{\cdot\cdot}$ and O_i'' are reversible depending on environmental conditions.[25] Thermal annealing is controlled before any heat-induced degradation of PCE occurs, which is optimized by varying the time and temperature in N_2 condition (Figure S9).

We then focus on the 20-nm SnO_x and show in Figures 3C–3E the statistical data of V_{OC}, FF, and PCE depending on SnO_x's WF. A clear difference is immediately seen: the Ag device shows a small reduction in PCE with increasing WF, while both Au devices and carbon devices exhibit a more pronounced decline in PCE with increased WF. The change of PCE is primarily caused by variation in FF, instead of by change in V_{OC}. An inspection of the representative JV curves, Figures 3F–3H, reveals

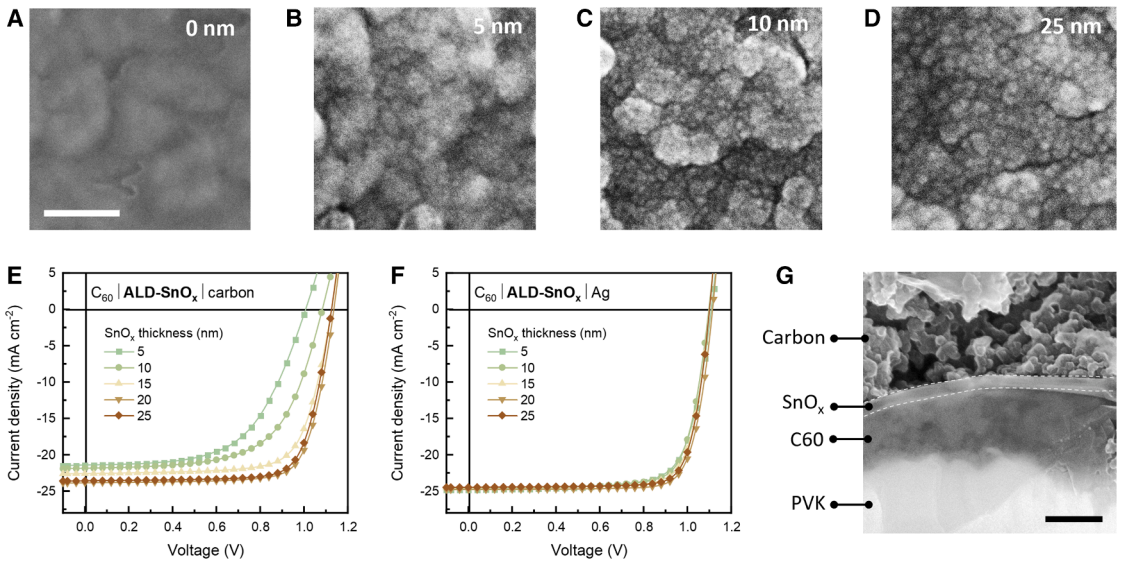

Figure 2. Impact of SnO_x thickness on device performance

(A–D) Surface SEM images of SnO_x films deposited on C60 substrate with different SnO_x thickness. The scale bar represents 100 nm.

(E and F) Representative JV curves of p-i-n PSCs comprising ALD-SnO_x interlayer of varied thickness with (E) carbon electrode (E) and Ag electrode (F).

(G) Cross-sectional SEM images of a perovskite (PVK)/C60/SnO_x/carbon interface. Here, a C_{60} layer with thickness greater than optimized value is deposited for the ease of image acquisition. The scale bar represents 100 nm.

that the reduced FF in Au-PSC and carbon-PSC is associated with the emergence of an "s-shaped" curve, which suggests the formation of Schottky barrier at one or multiple interfaces impeding charge extraction.[26,27] It is worth noting that carbon and Au devices exhibit nearly comparable $V_{OC} \times$ FF products, despite a difference in J_{SC} (Figure S10) leading to slightly lower PCE for the former. This means, for high-WF electrodes, electron extraction is highly sensitive to doping and thereby the WF of the interlayer, which will be explained in detail below.

Origin of enhanced electron extraction to carbon

Having established the WF of SnO_x as a practical QC metric, we then probed how SnO_x/carbon band alignment evolves to clarify the origin of efficient electron extraction to carbon. First, the stoichiometric variation in bulk SnO_2 as a result of oxygen vacancy tuning is characterized with X-ray photoelectron spectroscopy (XPS), measuring the survey spectra and core-level spectra of O 1s and Sn 3d (see Figures S11 and S12), which allows for rapid determination of O/Sn atomic ratios by integration of O 1s and Sn 3d peaks using corresponding relative sensitivity factors. Figure 4A shows that the as-deposited SnO_x is moderately oxygen deficient (x = 1.95) in the absence of post-treatments,[28] and it becomes more so when treated in N_2 atmosphere (x = 1.84), leading to strong n-type self-doping. On the contrary, treatment in air incorporates oxygen in the lattice, and the film becomes more stoichiometric and even slightly rich in oxygen (x = 2.09), resulting in a reduction in n-doping. The valence band (VB) spectra feature a negligible shift of VB maximum (Figure S13), though. These results suggest formation of $V_O^{\cdot\cdot}$ by post-treatment varying O/Sn ratio as the main cause of WF change, which is consistent with our hypothesis on the management of oxygen, shown in Figure 3A.

To elucidate how interfacial band alignment evolves, we show in Figure 4B the change of WF of SnO_x deposited on an ITO substrate, with varied thickness from 3 to 10 nm. Because ITO (WF = 4.93 eV) forms a Schottky contact with SnO_x, which resembles carbon (WF = 4.82 eV), ultra-thin SnO_x is fully depleted, and its measured WF tracks ITO's surface potential. As thickness increases, the measured WF relaxes exponentially toward bulk SnO_x's value and eventually remains unchanged when it is greater than the depletion (space-charge) width of SnO_x (schematically drawn in Figure S14). The built-in potential of the interface, namely, the total drop of WF, excellently matches the WF offsets between ITO and SnO_x: ~0.60 eV for N_2-annealed SnO_x, ~0.50 eV for as-deposited SnO_x, and ~0.20 eV for air-annealed SnO_x.

These results allow us to estimate the Debye length (L_D) and thus the carrier density of the SnO_x films:

$$\phi(x) = \phi_{SnO_x,bulk} + \Delta\phi \exp\left(-\frac{x}{L_D}\right), \qquad \text{(Equation 2)}$$

$$L_D = \sqrt{\frac{\varepsilon_r \varepsilon_0 kT}{q^2 n}}, \qquad \text{(Equation 3)}$$

where $\phi(x)$ is the measured WF at position x, $\phi_{SnO_x,bulk}$ is the WF of bulk SnO_x, and $\Delta\phi$ is the total WF difference. T is temperature (300 K), q is the unit charge (1.602×10^{-19} C), ε_0 is vacuum permittivity (8.85×10^{-14} F cm^{-1}), and ε_r is the relative permittivity of SnO_2 (9–12).[29] Fitting the WF thickness data with single exponential (shown on Figure 4B) yields L_D of 0.6 nm (N_2-annealed), 2.9 nm (as-deposited), and 4.3 nm (air-annealed), showing a progressive widening of depletion region. Using L_D,

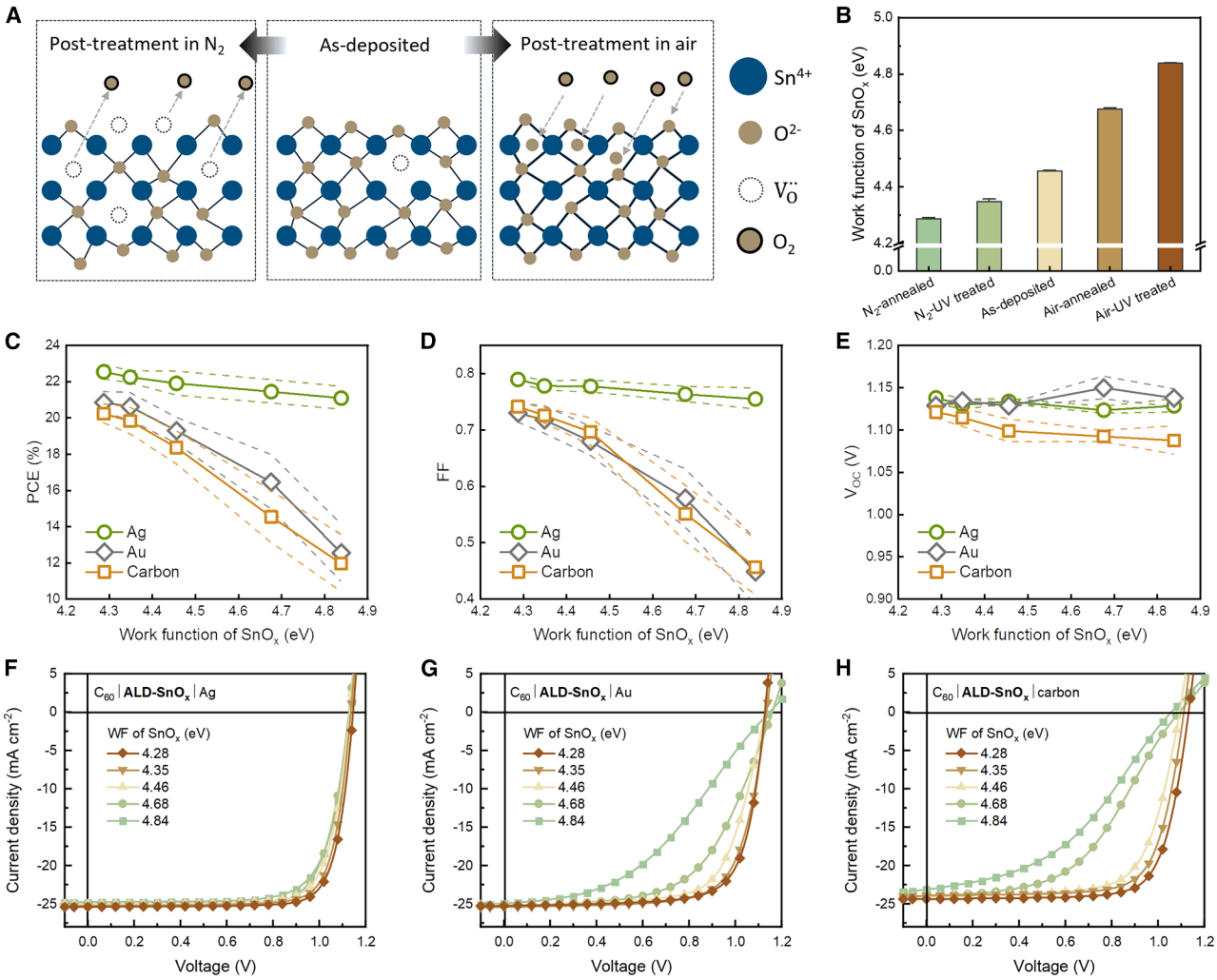

Figure 3. Tuning SnO_x's WF and its impact on device performance

(A) Schematic drawing of controlling oxygen vacancies in the lattice of SnO_2 through post-deposition treatments in ambient air and in N_2 atmosphere.

(B) Impact of post-deposition treatments on the WF of SnO_x film, measured with a Kelvin probe.

(C–E) Statistical data of the dependence of PCE (C), FF (D), and V_{OC} (E) on the WF of SnO_x in the p-i-n PSCs with Au, Ag, and carbon electrodes, respectively, measured from 15 devices for each condition. The dashed lines represent the error bar of the statistical data.

(F–H) Representative plots showing the dependence of JV curves on the WF of SnO_x interlayer in PSC with Au, Ag, and carbon electrodes, respectively.

we are able to estimate carrier density n in the SnO_x films; this gives an approximate value of 3.6–4.8 $\times$ 10^{19} cm^{-3} for N_2-annealed SnO_x, which is orders of magnitude higher than that of as-deposited SnO_x (1.53–2.04 $\times$ 10^{18} cm^{-3}) and air-annealed SnO_x (7.0–9.3 $\times$ 10^{17} cm^{-3}). These results suggest narrowing of the depletion region and an increase in charge density in the N_2-annealed SnO_x, as compared with as-deposited or air-annealed ones, as a result of self-doping by oxygen vacancies.

The consequence of narrowed depletion region can be seen from measuring the current-voltage (IV) characteristics of an ITO/SnO_x/carbon Schottky diode, Figure 4C. The key observation from the IV curve of the air-annealed SnO_x is a strong diode characteristic and a moderate asymmetry between electron injection from carbon and from ITO, which leads to significantly lower current injection in the low-bias region (see also Figure S15). By contrast, the diode characteristics diminish in the device with as-deposited SnO_x and become nearly linear with N_2-annealed SnO_x. These results suggest non-negligible injection barriers and thus greater contact resistance at both ITO- and carbon-interface when SnO_x is subject to annealing in air, whereas the contact becomes nearly ohmic with annealing in N_2.

The above results allow us to schematically draw the energy diagram in Figure 4D: when bringing SnO_x in contact with a high-WF electrode, a Schottky contact is formed but the profile of the band bending depends strongly on the self-doping of SnO_2—n-type self-doping of SnO_2 toward SnO_{2-x} shifts its Fermi level upward to the conduction band (CB), resulting in both greater interfacial bending and reduced depletion width with high-WF electrode. This eventually leads to the alignment

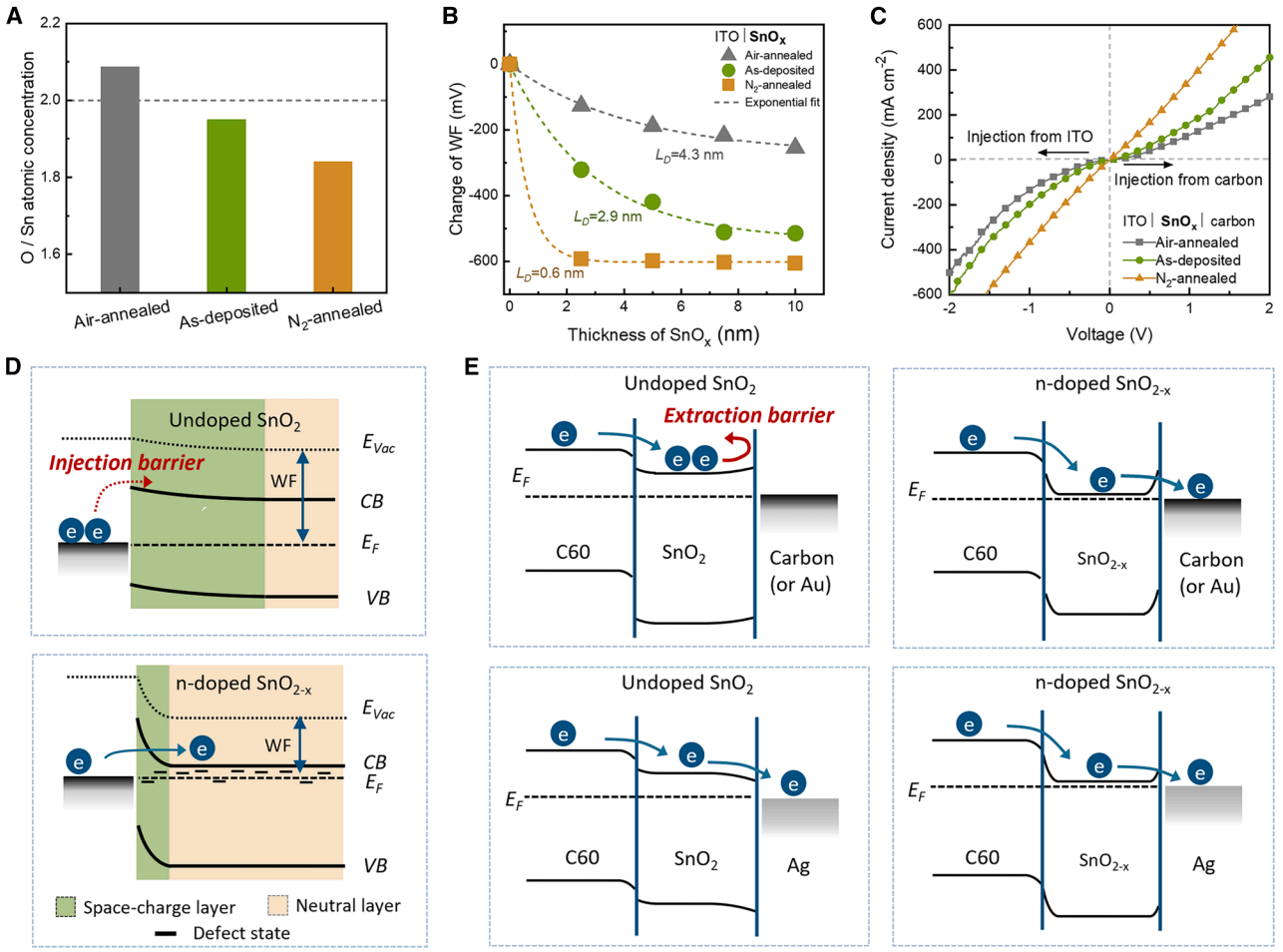

Figure 4. Impact of SnO_x self-doping on interfacial band alignment

(A) Atomic concentration ratio of O and Sn in SnO_x films after different post-deposition treatments.

(B) WF change of SnO_x films deposited on ITO substrates, with varied thickness from 3 to 10 nm and different post-deposition treatments. The data are an average of 6 measurements from different positions.

(C) IV curves of ITO/SnO_x/carbon Schottky diodes.

(D) Schematic drawing showing the impact of SnO_x's self-doping on interfacial band bending, formation of space-charge layer, and electron injection in a Schottky contact with a high-WF electrode.

(E) Schematic drawing of the band profile at C_{60}/SnO_x/electrode interface with undoped SnO_2 and n-doped SnO_{2-x}.

of the electrode's Fermi level to SnO_{2-x}'s CB and, more importantly, allows electrons to tunnel through the narrow space-charge layer. By contrast, the larger energy-level offset and the wider space-charge layer formed with intrinsic SnO_2 noticeably impede electron injections.

We further correlate the change of injection barrier to the variation of electron-extraction barrier, by plotting in Figure 4E the band profiles of C_{60}/SnO_x/electrode interface: undoped SnO_2 forms ohmic contact with Ag but Schottky contacts with carbon (or Au). The Schottky contact hinders electron extraction, leads to electron accumulation at the interfaces, and eventually results in s-shaped JV curves as observed in Figures 3G and 3H.[30] It herein presents a classical Schottky challenge to form semi-metallic contact between a metal and a semiconductor with significant energetic offsets, which can be resolved with a heavily n-doped SnO_{2-x}: band bending becomes greater at both C_{60}/SnO_{2-x} and SnO_{2-x}/carbon interfaces, and the Fermi level of carbon (or Au) is brought close to the CB of SnO_{2-x}. The narrowed depletion region allows for electron tunneling through the Schottky barrier, resulting in a quasi-ohmic contact between SnO_{2-x}/carbon (or Au). We note that in all cases, the Fermi levels of the electrodes align with that of C_{60}, thus the built-in potential of the solar cell remains unchanged regardless of the WF variations from SnO_x or electrodes. This is in excellent agreement with our JV measurements (Figures 3F–3H) showing the main loss of PV parameters to be FF, while the loss of V_{OC} remains trivial.

Techno-economic analysis of carbon-electrode p-i-n PSC

Having shown that a mechanically robust ALD interlayer is compatible with printing of carbon and that self-doping of SnO_x enables efficient electron extraction to carbon, we now

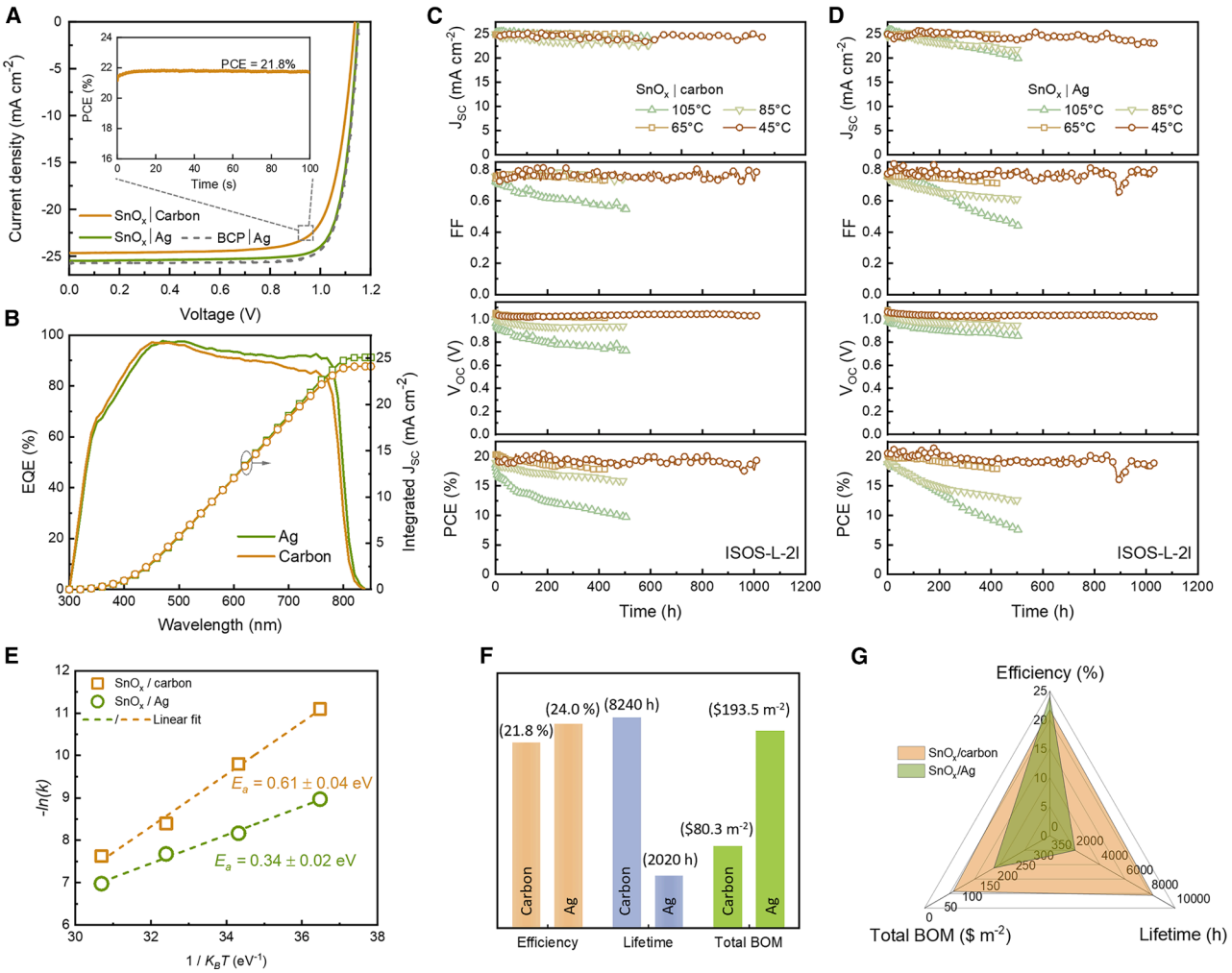

Figure 5. Assessment of the efficiency-lifetime-cost balance

(A) JV characteristics of the champion solar cells with SnO_x/carbon, SnO_x/Ag, and BCP/Ag electrode, respectively. The inset figure shows the stabilized PCE of the champion SnO_x/carbon device under maximum power point (MPP) tracking mode.

(B) EQE spectra and integrated J_{SC} of the champion solar cells with SnO_x/carbon electrode and SnO_x/Ag electrode, respectively.

(C and D) Evolution of J_{SC}, V_{OC}, FF, and PCE of the PSCs with SnO_x/Ag and SnO_x/carbon electrodes, all measured in a nitrogen-filled box under 1-sun equivalent illumination (provided by a metal-halide lamp with a UV filter) at 45°C, 65°C, 85°C, and 105°C, respectively.

(E) The logarithm of degradation rate ($ln(k)$) vs. the inverse of the thermal energy ($1/k_BT$) obtained from a linear fit to the degradation curve from the time later than 100 h.

(F) Column plot of champion PCE, predicted T_{80} lifetime at 30°C, and total BOM between SnO_x/Ag and SnO_x/carbon electrodes.

(G) Efficiency-stability-cost balance in the "golden triangle" of PSCs with SnO_x/Ag and SnO_x/carbon electrodes.

examine how integrating a carbon cathode reshapes the efficiency-longevity-cost balance in p-i-n PSCs, the key determinant of economic viability. First, the investigation of SnO_x self-doping enables us to rationally optimize device fabrication and to show, in Figure 5A, the JV curves of the champion-performing ones; the champion carbon-PSC shows a J_{SC} of 24.7 mA cm^{-2}, V_{OC} of 1.138 V, FF of 77.8%, and PCE of 21.8%. Importantly, the device exhibits minimal hysteresis in the JV curve when scanning direction is reversed, with comparable JV parameters of 24.7 mA cm^{-2}, 1.134 V, and 77.1% and 21.6% obtained in forward-scan measurement (Figure S16). This leads to a stabilized PCE of 21.8%, measured with a maximum power point tracking protocol shown in the inset figure (see also Figure S17). The performance of carbon-PSC is benchmarked against the PSC with SnO_x/Ag cathode, and further against the "reference" p-i-n PSC with BCP/Ag cathode, with the JV curves of their respective champion devices also plotted in Figure 5A, showing the following: J_{SC} of 25.5 and 25.7 mA cm^{-2}, V_{OC} of 1.151 and 1.155 V, FF of 81.8% and 82.5%, and PCE of 24.0% and 24.5%, for SnO_x/Ag-PSC and BCP/Ag-PSC, respectively.

To further elucidate the PCE gap between evaporated and printed electrode, we list in Table 1 the statistical data of PV parameters for SnO_x/carbon, SnO_x/Ag, and BCP/Ag, collected from the best-performing fabrication batch (see boxplot in

Table 1. PV parameters of p-i-n PSCs with different cathodes

Device	Condition	J_{SC} (mA cm^{-2})	V_{OC} (V)	FF (%)	PCE (%)
SnO_x/carbon	champion	24.7	1.138	77.8	21.8
	average	24.3 ± 0.3	1.129 ± 0.005	77.0 ± 1.0	21.1 ± 0.5
SnO_x/Ag	champion	25.5	1.151	81.8	24.0
	average	25.5 ± 0.3	1.143 ± 0.003	80.8 ± 0.7	23.5 ± 0.4
BCP/Ag	champion	25.7	1.155	82.5	24.5
	average	25.5 ± 0.2	1.146 ± 0.009	81.7 ± 0.7	23.9 ± 0.5

Data for each condition are measured from 10 pixels of 2 devices made within the same batch.

Figure S18). The data show a small loss of PCE of 0.4% by replacing BCP with SnO_x and a loss of 2.8% when employing carbon electrode. Although silver-to-carbon loss of PCE is minimized by tailoring SnO_x interlayer, the PCE of carbon-PSC may be further improved through the optimization of our reference device, which is yet to become state of the art. Nevertheless, to the best of our knowledge, this is not only one of the first reports of p-i-n PSCs using only printed carbon as rear electrode but is also among the highest reported stabilized PCEs of carbon-PSCs.

Figure 5B shows the external quantum efficiency (EQE) spectra of the champion devices, showing a good match between the integrated J_{SC}s and the measured ones, which are 24.1 vs. 24.7 mA cm^{-2} for carbon and 25.1 vs. 25.5 mA cm^{-2} for Ag. The EQE spectra, however, highlight a rooted loss of J_{SC} with carbon electrode caused by reduced conversion of the long-wavelength photons. Because perovskite absorption is weak at long wavelengths, the device photocurrent becomes reflectance limited[31]; the lower back reflectance of the carbon contact reduces the optical path length, lowering EQE in the 750–1,000 nm band.[32] In this regard, we maximized perovskite thickness within our fabrication recipe, which partially compensates for this effect (Figure S19) but cannot fully offset the reflectance difference.

One of the most intriguing properties of the carbon electrode is its chemical inertness that can largely mitigate electrode-induced degradation.[11] This is more so when carbon can be used as an alternative to Ag. We therefore turn to characterize the stability of PSCs with SnO_x/carbon and SnO_x/Ag and show in Figures 5C and 5D the evolution of the PV parameters under accelerated aging conditions. The aging is carried out under continuous 1-sun equivalent illumination in an N_2-filled chamber, with the PSCs operating at 45°C, 65°C, 85°C, and 105°C, the so-called International Summit on Organic/Hybrid PV Stability – Light-soaking – Level 2 – Inert (ISOS-L-2I) testing protocol.[33] Neither of the degradation curves is strictly linear, with the decay in the initial few hours showing different kinetics from decay afterward; we focus on the slower decay herein, as it is more relevant to long-term operational stability. This can be quantified with a temperature-dependent constant k describing the rate of PCE decrease over time (Figures S20 and S21):

$$\mathrm{PCE}(t) = k(T)t + B \qquad \text{(Equation 4)}$$

where t is aging time, PCE(t) is the measured PCE at certain aging time t, T is temperature, and B is a constant. We assume an Arrhenius model to describe $k(T)$, which allows us to estimate the activation energy (E_a) of PSC degradation:

$$k(T) = A\exp\left(-\frac{E_a}{k_B T}\right) \qquad \text{(Equation 5)}$$

where k_B is the Boltzmann's constant, and A is a constant that includes the impact of light and voltage on degradation rate, which are otherwise fixed in our test. In Figure 5E, we plot the logarithm of degradation rate ($ln(k)$) vs. the inverse of the thermal energy ($1/k_BT$). A good linearity can be observed from both the data of SnO_x/carbon and SnO_x/Ag, which means $k(T)$ can be adequately described by an Arrhenius function across the temperature range. In this regard, E_a can be estimated from the slope of a linear fit to the data, which is 0.61 ± 0.02 eV for SnO_x/carbon, nearly twice of that of 0.34 ± 0.02 eV for SnO_x/Ag.

The linear correlation is indicative of the degradation of PSCs being dominated by a single, thermally activated physical process, very likely to be the diffusion of ionic species.[28] Importantly, an E_a of 0.62 eV is very close to the reported formation energy of iodine vacancies, which is 0.55–0.6 eV for CsFA-based perovskite,[34,35] implying carbon-PSCs' lifetimes being limited by the degradation of bulk perovskite and SnO_x/carbon playing a negligible role in device degradation. By contrast, an E_a of 0.34 eV for SnO_x/Ag, lower than typical activation energy of defects, suggests corrosion of interfaces or electrode as an accelerating factor of device degradation.

SnO_x/Ag contact was previously used as an alternative to BCP/Ag to gain longevity of the solar cell in spite of a small sacrifice in cell efficiency.[36,37] On this basis, our results suggest that carbon could further extend device longevity by largely mitigating electrode-interface degradation, leaving the solar cell dominated by bulk degradation. By contrast, BCP/Ag contact in our case shows not only much faster degradation (Figure S22) but also a non-linear relationship between $ln(k)$ and $1/k_BT$ (Figure S23), meaning that no adequate description of $k(T)$ can be made by an Arrhenius function. This suggests one or multiple additional processes besides electrode corrosion causing the catastrophic device degradation, which is attributed to the well-known aggregation of BCP that is accelerated by elevation of temperature.[38]

With the known E_a's, we are able to use Equation 5 to estimate the degradation rate of the PSCs at standard operating temperature from the data measured at elevated temperature, leveraging an accelerating factor that describes the ratio between them (Figure S24), which allows us to calculate the equivalent aging time at 30°C from the data measured at

elevated temperatures (Figure S25). In Figure 5F, we plot the predicted T_{80} lifetime at 30°C, referred to as the aging time at which the PSC maintains 80% of the initial PCE, which is 8,240 h for SnO_x/carbon vs. 2,020 h for SnO_x/Ag, respectively.

Figure 5F also shows the total bill of materials (BOM) of the p-i-n PSC with Ag and carbon electrode, estimated directly using the model developed by Li and Chen.[39] In commercialized production, the material cost of carbon (0.01–0.02 \$ g^{-1}) is trivial compared with that of silver (0.7–1 \$ g^{-1}), which brings about a reduction of total BOM of the PSC from 193.5 \$ m^{-2} for Ag to 80.3 \$ m^{-2} for carbon. Beyond BOM, the embodied energy, referred to as the energy needed to produce a kilogram of the material, is drastically higher for silver (1,500 MJ kg^{-1}) than graphite (~40–50 MJ kg^{-1}). Replacing Ag with printed carbon reduces the upstream energy required for the rear electrode. Besides, because ALD-SnO_xnO_x adds negligible variable costd is tool-time limited, while Ag rear contacts are materials dominated, replacing Ag with printed carbon plus ALD-SnO_x shifts cost control from silver feedstock to process throughput.

With these results, we conclude by showing in Figure 5G the balance between efficiency, stability, and cost, referred to as the ''golden triangle'' of solar cells. It shows that replacing Ag with printed carbon electrodes trades a small PCE loss of 10% for a 300% enhancement of longevity and a 60% reduction in material cost. The enlarged triangle using carbon electrode presents a remarkable improvement in the economic viability of p-i-n PSCs.

DISCUSSION

Prior work has leveraged ALD layers for printed electrodes[40] and a variety of perovskite-based tandem devices,[41] with very recent work showing the compatibility of ALD-SnO_x with carbon.[42,43] Our work provides insights into metal/semiconductor contact physics, mechanistically elucidating how to convert the high-WF carbon from a conventional anode to a cathode with minimized charge-extraction loss. Unlike n-i-p architecture in which carbon is compatible with a variety of HTLs[11] or even an HTL-free interface,[12] p-i-n configuration shows a much stricter requirement of the interlayer's electronic properties; we identify narrowing of depletion region (reduced Debye length) key to enabling efficient electron extraction through SnO_x/carbon Schottky barrier, and we articulate a process-agnostic design rule to n-dope SnO_x interlayer and to use the WF of SnO_x as a quantifiable QC metric for the contact.

The polarity inversion is a contact-physics outcome, not a strategy-exclusive trick—any route that yields robust and n-type SnO_x (or an analogous oxide) should reproduce the effect, such as H_2/forming-gas treatment[44] and dipole[45] or amine-based surface modifier.[46] The same contact concept is also promising for metal-free interconnects that incorporate an ALD-SnO_x layer in tandems. While our experiments used a temporal ALD for proof-of-concept study, spatial ALD designed for high-throughput web processing in roll-to-roll production provides a credible upscaling pathway.[47] The identical surface chemistry of temporal and spatial ALD assures good transferability of our proposed SnO_x/carbon contact to industrial production.

Conclusions

Carbon demonstrates intriguing properties as the rear electrode of n-i-p PSCs, but its broader application in p-i-n PSCs has been prohibited. Our work addressed such deficiency, showing the first demonstration of carbon as an electron-collecting rear cathode. We identified the key challenges as (1) maintaining the integrity of the underlying interlayer against mechanical and chemical stresses from the printing of carbon paste and (2) resolving the rooted Schottky barrier problem between ETL and carbon. These are respectively resolved by ALD of robust thin-film SnO_x and by post-treatment controlling the oxygen vacancies in the SnO_x. The tailored interlayer allows us to reduce the PCE gap—though, not completely closing it—between PSC with carbon and Ag electrode. Considering the golden triangle of efficiency-stability-cost balance, this combination of competitive efficiency, enhanced stability, and substantial cost savings represents a viable pathway toward economically sustainable perovskite PVs.

METHODS

Materials

Lead iodide (PbI_2, 99.999%), lead bromide ($PbBr_2$, 99.999%), cesium iodide (CsI, 99.999%), N,N-dimethylformamide (DMF, anhydrous, ≥99.8%), dimethyl sulfoxide (DMSO, anhydrous, ≥99.9%), isopropanol (IPA, anhydrous, ≥99.8%), chlorobenzene (CB, anhydrous, 99.8%) were purchased from Sigma Aldrich. Methylammonium bromide (MABr, 99.99%), methylammonium chloride (MACl, 99.99%), formamidinium iodide (FAI, 99.99%), and phenethylammonium iodide (PEAI, 99.9%) were purchased from Great Cell Solar. NiO_x nanoparticle dispersion was purchased from Lumtech. Buckminsterfullerene (C_{60}, 99.5%), Me-4PACz, and BCP (≥98%) were purchased from Ossila. SnO_x nanoparticle dispersion was purchased from Avantama.

Solution preparation

NiO_x nanoparticle dispersion was 5 mg mL^{-1} in mixture of water and IPA (v:v = 3:1) and was used as received. SAM solution was prepared by dissolving Me-4PACz directly in DMF with a concentration of 0.5 mg/ml without additional stirring or heating. Perovskite solution was prepared by co-dissolving 6.7 mg MABr, 8.8 mg MACl, 18.2 mg CsI, 196.1 mg FAI, 22 mg $PbBr_2$, and 572 mg PbI_2 in 865 μL of mixture of DMF and DMSO (v:v = 4:1), to formulate a 1.5 M precursor solution with nominal composition of $Cs_{0.055}MA_{0.047}FA_{0.898}Pb(I_{0.953}Br_{0.047})_3$. The solution was stirred at 60°C for 1 h to ensure full dissolution of the precursors, and it was infiltrated with a 0.45 μm polytetrafluoroethylene (PTFE) filter prior to use. Solution of PEAI was prepared by dissolving 0.5 mg mL^{-1} powder in anhydrous IPA, which was stirred at room temperature until full dissolution of the PEAI. BCP solution was prepared by dissolving 0.5 mg mL^{-1} powder in anhydrous IPA and was shaken at room temperature until full dissolution of the powder. SnO_x nanoparticles were received as 5%$_{wt}$ dispersion in butanol and were diluted to 1%$_{wt}$ and infiltrated with 0.45 μm PTFE filter prior to use.

Device fabrication

The ITO-coated glass substrates (1 × 1 inch) were cleaned using deionized water, acetone, and IPA for 30 min in total

(10 min each) in the given order. Afterward, the substrates were dried with compressed air and were treated with UV-ozone for 20 min prior to layer coating.

NiO_x layer was deposited by spin coating 80 μL of the dispersion on the substrate at 2,000 rpm for 30 s, followed by thermal annealing on 150°C hot plate for 30 min. The substrates were then transferred into a nitrogen-filled glovebox for subsequent layer deposition. The SAM layer was prepared by spin coating 80 μL of the solution on NiO_x at 2,000 rpm for 30 s, followed by thermal annealing on 100°C hot plate for 10 min. The perovskite layer was deposited by spin coating 140 μL of precursor solution at 400 rpm for 15 s, followed by 32 s at 4,000 rpm. At the 17th second of 4,000-rpm spinning stage, 170 μL CB was dripped onto the spinning substrate as antisolvent, with a controlled speed of 150 μL s^{-1}. The film was then transferred onto a hot plate set at 120°C for 10 min. PEAI layer was deposited by spin coating 80 μL of solution at 3,000 rpm for 30 s, using dynamic mode, and then annealed at 100°C for 5 min. All the above coating processes were performed on a SPINBOT automatic spin-coating platform without manual operation. The time and speed of antisolvent dripping and the time of thermal annealing were both digitally controlled.

The samples were then transferred to an evaporator, in which 25 nm of C_{60} layer was thermally evaporated onto the perovskite with an average deposition rate of 0.2 Å/s and at pressures below 10^{-6} mbar. Afterward, the samples were moved to an ALD setup. The SnO_x layer was deposited onto C_{60} using low-temperature ALD at 110°C. TDMASn (tetrakis-dimethylamino tin) was used as precursor (pulse 400 ms, exposure 7 s) and H_2O as reactant (pulse 100 ms, exposure 7 s), and the reaction was run for 130 cycles. Precursor was heated to 65°C and oxidizer was at room temperature, while respective manifold temperatures for the precursor and oxidizer were 100°C and 80°C. The samples were then subjected to different post-deposition treatments prior to the deposition of electrodes.

As a replacement for ALD-SnO_x, a thin layer of BCP or SnO_x nanoparticles was deposited onto C_{60}, both by spin coating 80 μL of the solution (or the dispersion) at 3,000 rpm for 30 s followed by annealing at 100°C for 5 min.

To complete device fabrication, carbon electrodes were printed from a commercial paste (Liaoning Huite) on the SnO_x. The pixel shape was defined with a laser-patterned tape mask. The pixel area was defined to be 0.1 cm^2 (0.2 × 0.5 cm) and was checked by optical microscope. Wet carbon paste was subsequently annealed on a hot plate at 110°C for 15 min in ambient fume hood to be fully solidified. The thickness is approximately 20 μm, with sheet resistance below 10 Ω/square. Alternatively, 100 nm Ag or 60 nm Au was thermally evaporated onto the device, with an average deposition rate of 0.2 Å/s and at pressures below 10^{-6} mbar. The devices were covered by a square mask with a defined pixel area of 0.06 cm^2 during evaporation.

Characterizations

JV measurement

JV curves were measured using a Keithley source meter in ambient conditions (20°C–25°C). The illumination was provided by a Wavelab LED solar simulator with an embedded recipe of AM 1.5G spectrum and 100 mW cm^{-2}. The light intensity was calibrated with a crystalline Si cell. The JV curves were measured by applying bias from both −0.2 to 1.2 V (forward scan) and 1.2 to −-0.2 V (reverse scan) at a scan speed of 40 mV s^{-1}.

EQE measurement

The EQE spectra were measured with a commercial measurement system (Enlitech, QE-R). The incident light intensity at each wavelength was calibrated with a standard Si reference cell.

MPP measurement

The stabilized PCE was measured with MPP tracking software with embedded algorithm to determine the MPP of the device. The PCE data were obtained by measuring the photocurrent at given voltages.

Stability measurement

Aging of the solar cells was carried out with an ISOS-L-2I protocol, namely, in a nitrogen-filled chamber with glass window. The temperature in the chamber was adjusted by an underneath hot plate and was calibrated with a thermal couple. The continuous illumination was provided with a metal-halide lamp, and a UV filter was placed in front of the solar cells. The light intensity was approximately 1 sun equivalent and was continuously monitored by a photodiode sensor. The solar cells were held at a fixed voltage that is close to the voltage of their MPPs. JV scans (in both forward-scan and reverse-scan direction) were carried out periodically (approximately every 20 min) to determine the PCEs of the solar cells.

Thickness measurement

Thickness of the ALD SnO_x layers were measured using SENpro Spectroscopic ellipsometer with a tungsten halogen lamp. Silicon wafers with [100] direction and a SiO_2 layer of about 3 nm were used as the substrates for thickness measurements. Wafers were treated with UV light to clean the substrate surface and to generate hydroxyl group sites at SiO_2 surface to accommodate precursor adsorption at the surface. Predetermined material models with appropriate parameters were utilized to obtain the final thickness value from the measured spectra.

Kelvin probe measurement

WF was measured with a SPS040 instrument from KP Technology. The tip's WF was determined before the measurements, using a freshly cleaved highly ordered pyrolytic graphite (HOPG) sample for calculating the absolute WF value.

XRD and SEM measurements

Crystallographic information of the thin films was obtained with a Panalytical X'pert powder diffractometer (Cu-Kα radiation, λ = 0.154 nm) and an X'Celerator solid-state stripe detector with conditions of 40 kV and 30 mA. Surface morphologies of the SnO_x films were investigated by a JEOL (JSM-7610F) SEM.

XPS measurement

XPS characterization was carried out with the aid of a Quantera II (Physical Electronics, Chanhassen, MN, USA) device, equipped with a monochromatic Al Kα-X-ray source (1,486.6 eV), which was operated at 15 kV and 25 W. Analysis of the spectra was carried out using the software Casa XPS (http://www.casaxps.com/). The surface composition of each sample was obtained by the integration of the Sn 3d and O 1s peaks, using corresponding relative sensitivity factors. The atomic ratios presented in the manuscript feature only Sn and O in atomic percent, omitting other chemical elements.

RESOURCE AVAILABILITY

Lead contact

Requests for further information and resources should be directed to and will be fulfilled by the lead contact, Christoph J. Brabec (christoph.brabec@fau.de).

Materials availability

This study did not generate new unique reagents.

Data and code availability

This study did not generate any datasets or code.

ACKNOWLEDGMENTS

The authors acknowledge financial support from the Bavarian State Government (FKZ 20.2-3410.5-4-5), from Deutsche Forschungsgemeinschaft (DFG) via the Perovskite SPP2196 program (project no. 506698391), from the Bavarian-Czech Academic Agency (BTHA) via the project "BaCzALD – Bavarian-Czech alliance for photoactive films by solution atomic layer deposition" (grant no. BTHA-JC-2024-2), from Deutsche Forschungsgemeinschaft (DFG) within the Collaborative Research Center "ChemPrint" (project 538767711, CRC 1719), and from Helmholtz-Gemeinschaft Deutscher Forschungszentren via the project "Zeitenwende." The authors acknowledge the support provided by the Helmholtz Association, in the framework of the innovation platform "Solar TAP," and by the "Solar Factory of the Future," an initiative under the cooperation between FAU (i-MEET) and FZJ (HI ERN) that is located at the Energy Campus Nürnberg (EnCN). Z.P., S.Q., and L.D. acknowledge support from the China Scholarship Council (CSC).

AUTHOR CONTRIBUTIONS

T.D. and H.U.D. contributed equally. T.D. and C.J.B. conceived the idea. T.D. designed the experiments and wrote the manuscript. H.U.D. optimized ALD and carried out device fabrication and WF measurement. Z.P. set up the stability measurement. J.E. assisted with ALD optimization and was supervised by J.B. A.B. took SEM images. H.Z., J.Z., and J.T. optimized inverted PSC fabrication. S.Q., L.D., and M.W. assisted with the optimization of carbon-PSC. O.K. carried out XPS measurement and data analysis. F.G. contributed to conceptualization. J.A.H. and C.J.B. directed the project and supervised this study. All authors discussed the results and commented on the manuscript.

DECLARATION OF INTERESTS

T.D., H.U.D., and C.J.B. are filing a patent based on this work.

SUPPLEMENTAL INFORMATION

Supplemental information can be found online at https://doi.org/10.1016/j.joule.2025.102224.

Received: June 27, 2025
Revised: September 8, 2025
Accepted: October 30, 2025
Published: December 5, 2025

REFERENCES

1. Parvazian, E., and Watson, T. (2024). The roll-to-roll revolution to tackle the industrial leap for perovskite solar cells. Nat. Commun. *15*, 3983. https://doi.org/10.1038/s41467-024-48518-4.
2. Qiu, S., Majewski, M., Dong, L., Jang, D., Corre, V.M.L., Cerrillo, J.G., Ronsin, O.J.J., Yang, F., Guo, F., Zhang, K., et al. (2024). In Situ Probing the Crystallization Kinetics in Gas-Quenching-Assisted Coating of Perovskite Films. Adv. Energy Mater. *14*, 2303210. https://doi.org/10.1002/aenm.202303210.
3. Du, T., Rehm, V., Qiu, S., Pal, S., Jang, D., Peng, Z., Zhang, J., Yuan, H., Briscoe, J., Heiss, W., et al. (2024). Precursor-Engineered Volatile Inks Enable Reliable Blade-Coating of Cesium–Formamidinium Perovskites Toward Fully Printed Solar Modules. Adv. Sci. (Weinh) *11*, e2401783. https://doi.org/10.1002/advs.202401783.
4. Dong, L., Qiu, S., García Cerrillo, J., Wagner, M., Kasian, O., Feroze, S., Jang, D., Li, C., Peisert, H., Zhang, K., et al. (2024). Fully printed flexible perovskite solar modules with improved energy alignment by tin oxide surface modification. Energy Environ. Sci. *17*, 7097–7106. https://doi.org/10.1039/D4EE01647E.
5. Sutherland, L.J., Vak, D., Gao, M., Peiris, T.A.N., Jasieniak, J., Simon, G.P., and Weerasinghe, H. (2022). Vacuum-Free and Solvent-Free Deposition of Electrodes for Roll-to-Roll Fabricated Perovskite Solar Cells. Adv. Energy Mater. *12*, 2202142. https://doi.org/10.1002/aenm.202202142.
6. Beynon, D., Parvazian, E., Hooper, K., McGettrick, J., Patidar, R., Dunlop, T., Wei, Z., Davies, P., Garcia-Rodriguez, R., Carnie, M., et al. (2023). All-Printed Roll-to-Roll Perovskite Photovoltaics Enabled by Solution-Processed Carbon Electrode. Adv. Mater. *35*, e2208561. https://doi.org/10.1002/adma.202208561.
7. Kajal, P., Verma, B., Vadaga, S.G.R., and Powar, S. (2022). Costing Analysis of Scalable Carbon-Based Perovskite Modules Using Bottom Up Technique. Glob. Chall. *6*, 2100070. https://doi.org/10.1002/gch2.202100070.
8. Dong, L., Qiu, S., Feroze, S., Wagner, M., Kasian, O., Peisert, H., Kosasih, F.U., Ducati, C., Garcia Cerrillo, J., Tian, J., et al. (2024). Simplifying contact-layer design for high-throughput printing of flexible perovskite photovoltaics. Energy Environ. Sci. *17*, 7147–7154. https://doi.org/10.1039/D4EE02707H.
9. Tong, J., Dong, C., Yao, M., Wang, Q., Shen, C., Yue, Y., Yan, L., Gao, Y., Yue, G., Zhang, W., et al. (2025). 22.1% Carbon-Electrode Perovskite Solar Cells by Spontaneous Passivation and Self-Assembly of Hole-Transport Bilayer. ACS Nano *19*, 12960–12970. https://doi.org/10.1021/acsnano.4c16916.
10. Xie, H., Lei, J., Zhu, Z., Xu, X., Li, D., Xu, J., Pan, Y., and Yin, X. (2025). Practical Interface Engineering between Perovskite and Carbon Electrode in Regular Carbon-Based Perovskite Solar Cells. ACS Appl. Mater. Interfaces *17*, 33271–33295. https://doi.org/10.1021/acsami.4c20906.
11. Du, T., Qiu, S., Zhou, X., Le Corre, V.M., Wu, M., Dong, L., Peng, Z., Zhao, Y., Jang, D., Spiecker, E., et al. (2023). Efficient, stable, and fully printed carbon-electrode perovskite solar cells enabled by hole-transporting bilayers. Joule *7*, 1920–1937. https://doi.org/10.1016/j.joule.2023.06.005.
12. Zouhair, S., Kim, H., Bogachuk, D., Philipp Herterich, J., Lim, J., Yoo, S.-M., Chahboun, A., Khaja Nazeeruddin, M., Hinsch, A., Wagner, L., et al. (2022). Employing 2D-Perovskite as an Electron Blocking Layer in Highly Efficient (18.5%) Perovskite Solar Cells with Printable Low Temperature Carbon Electrode. Adv. Energy Mater. *12*, 2200837. https://doi.org/10.1002/aenm.2022008370.
13. Tang, J., Lin, Y., Yan, H., Lin, J., Rao, H., Pan, Z., and Zhong, X. (2024). 20.1 % Certified Efficiency of Planar Hole Transport Layer-Free Carbon-Based Perovskite Solar Cells by Spacer Cation Chain Length Engineering of 2D Perovskites. Angew. Chem. Int. Ed. Engl. *63*, e202406167. https://doi.org/10.1002/anie.202406167.
14. Luo, X., Liu, X., Lin, X., Wu, T., Wang, Y., Han, Q., Wu, Y., Segawa, H., and Han, L. (2024). Recent Advances of Inverted Perovskite Solar Cells. ACS Energy Lett. *9*, 1487–1506. https://doi.org/10.1021/acsenergylett.4c00140.
15. Chen, P., Xiao, Y., Li, S., Jia, X., Luo, D., Zhang, W., Snaith, H.J., Gong, Q., and Zhu, R. (2024). The Promise and Challenges of Inverted Perovskite Solar Cells. Chem. Rev. *124*, 10623–10700. https://doi.org/10.1021/acs.chemrev.4c00073.

16. Lin, X., Cui, D., Luo, X., Zhang, C., Han, Q., Wang, Y., and Han, L. (2020). Efficiency progress of inverted perovskite solar cells. Energy Environ. Sci. *13*, 3823–3847. https://doi.org/10.1039/D0EE02017F.

17. Troughton, J., Neophytou, M., Gasparini, N., Seitkhan, A., Isikgor, F.H., Song, X., Lin, Y.H., Liu, T., Faber, H., Yengel, E., et al. (2020). A universal solution processed interfacial bilayer enabling ohmic contact in organic and hybrid optoelectronic devices. Energy Environ. Sci. *13*, 268–276. https://doi.org/10.1039/C9EE02202C.

18. Liu, L., Yu, B., Kang, L., Deng, W., and Zhao, X. (2023). Blade Coating of Alloy as Top Electrodes for Efficient All-Printed Organic Photovoltaics. Adv. Funct. Mater. *33*, 1–11. https://doi.org/10.1002/adfm.202214781.

19. Guo, F., Azimi, H., Hou, Y., Przybilla, T., Hu, M., Bronnbauer, C., Langner, S., Spiecker, E., Forberich, K., and Brabec, C.J. (2015). High-performance semitransparent perovskite solar cells with solution-processed silver nanowires as top electrodes. Nanoscale *7*, 1642–1649. https://doi.org/10.1039/c4nr06033d.

20. Margulis, G.Y., Christoforo, M.G., Lam, D., Beiley, Z.M., Bowring, A.R., Bailie, C.D., Salleo, A., and McGehee, M.D. (2013). Spray deposition of silver nanowire electrodes for semitransparent solid-state dye-sensitized solar cells. Adv. Energy Mater. *3*, 1657–1663. https://doi.org/10.1002/aenm.201300660.

21. Cheng, H.E., Tian, D.C., and Huang, K.C. (2012). Properties of SnO2 films grown by atomic layer deposition. Procedia Eng. *36*, 510–515. https://doi.org/10.1016/j.proeng.2012.03.074.

22. Zouhair, S., Clegg, C., Valitova, I., March, S., Jailani, J.M., and Pecunia, V. (2024). Carbon Electrodes for Perovskite Photovoltaics: Interfacial Properties, Meta-analysis, and Prospects. Sol. RRL *8*, 1–25. https://doi.org/10.1002/solr.202300929.

23. Batzill, M., and Diebold, U. (2005). The surface and materials science of tin oxide. Prog. Surf. Sci. *79*, 47–154. https://doi.org/10.1016/j.progsurf.2005.09.002.

24. Park, S.Y., and Zhu, K. (2022). Advances in SnO2 for Efficient and Stable n–i–p Perovskite Solar Cells. Adv. Mater. *34*, e2110438. https://doi.org/10.1002/adma.202110438.

25. Verbakel, F., Meskers, S.C.J., and Janssen, R.A.J. (2007). Electronic memory effects in diodes of zinc oxide nanoparticles in a matrix of polystyrene or poly(3-hexylthiophene). J. Appl. Phys. *102*, 083701. https://doi.org/10.1063/1.2794475.

26. Gupta, D., Mukhopadhyay, S., and Narayan, K.S. (2010). Fill factor in organic solar cells. Sol. Energy Mater. Sol. Cells *94*, 1309–1313. https://doi.org/10.1016/j.solmat.2008.06.001.

27. Tress, W., and Inganäs, O. (2013). Simple experimental test to distinguish extraction and injection barriers at the electrodes of (organic) solar cells with S-shaped current-voltage characteristics. Sol. Energy Mater. Sol. Cells *117*, 599–603. https://doi.org/10.1016/j.solmat.2013.07.014.

28. Jarzebski, Z.M., and Marton, J.P. (1976). Physical Properties of SnO2 Materials: I. Preparation and Defect Structure. J. Electrochem. Soc. *123*, 199C–205C. https://doi.org/10.1149/1.2133010.

29. Hu, Y., Hwang, J., Lee, Y., Conlin, P., Schlom, D.G., Datta, S., and Cho, K. (2019). First principles calculations of intrinsic mobilities in tin-based oxide semiconductors SnO, SnO2, and Ta2SnO6. J. Appl. Phys. *126*, 185701. https://doi.org/10.1063/1.5109265.

30. Wagenpfahl, A., Rauh, D., Binder, M., Deibel, C., and Dyakonov, V. (2010). S-shaped current-voltage characteristics of organic solar devices. Phys. Rev. B *82*, 1–8. https://doi.org/10.1103/PhysRevB.82.115306.

31. Du, T., Xu, W., Xu, S., Ratnasingham, S.R., Lin, C.T., Kim, J., Briscoe, J., McLachlan, M.A., and Durrant, J.R. (2020). Light-intensity and thickness dependent efficiency of planar perovskite solar cells: charge recombination versus extraction. J. Mater. Chem. C *8*, 12648–12655. https://doi.org/10.1039/D0TC03390A.

32. Qiu, S., Majewski, M., Dong, L., Distler, A., Li, C., Forberich, K., Tian, J., Hemasiri, N.H., Liu, C., Zhang, J., et al. (2025). Over one-micron-thick void-free perovskite layers enable highly efficient and fully printed solar cells. Energy Environ. Sci. *18*, 5926–5939. https://doi.org/10.1039/D5EE01722J.

33. Khenkin, M.V., Katz, E.A., Abate, A., Bardizza, G., Berry, J.J., Brabec, C., Brunetti, F., Bulović, V., Burlingame, Q., Di Carlo, A., et al. (2020). Consensus statement for stability assessment and reporting for perovskite photovoltaics based on ISOS procedures. Nat. Energy *5*, 35–49. https://doi.org/10.1038/s41560-019-0529-5.

34. Ming, W., Chen, S., and Du, M.-H. (2016). Chemical instability leads to unusual chemical-potential-independent defect formation and diffusion in perovskite solar cell material CH 3 NH 3 PbI 3. J. Mater. Chem. A *4*, 16975–16981. https://doi.org/10.1039/C6TA07492H.

35. Yin, W.-J., Shi, T., and Yan, Y. (2014). Unusual defect physics in CH3NH3PbI3 perovskite solar cell absorber. Appl. Phys. Lett. *104*, 063903. https://doi.org/10.1063/1.4864778.

36. Chen, H., Liu, C., Xu, J., Maxwell, A., Zhou, W., Yang, Y., Zhou, Q., Bati, A.S.R., Wan, H., Wang, Z., et al. (2024). Improved charge extraction in inverted perovskite solar cells with dual-site-binding ligands. Science *384*, 189–193. https://doi.org/10.1126/science.adm9474.

37. Li, C., Wang, X., Bi, E., Jiang, F., Park, S.M., Li, Y., Chen, L., Wang, Z., Zeng, L., Chen, H., et al. (2023). Rational design of Lewis base molecules for stable and efficient inverted perovskite solar cells. Science *379*, 690–694. https://doi.org/10.1126/science.ade3970.

38. Peumans, P., Yakimov, A., and Forrest, S.R. (2003). Small molecular weight organic thin-film photodetectors and solar cells. J. Appl. Phys. *93*, 3693–3723. https://doi.org/10.1063/1.1534621.

39. Li, G., and Chen, H. (2024). Manufacturing Cost Analysis of Single-Junction Perovskite Solar Cells. Sol. RRL *8*, 2400540. https://doi.org/10.1002/solr.202400540.

40. Gahlmann, T., Brinkmann, K.O., Becker, T., Tückmantel, C., Kreusel, C., van gen Hassend, F., Weber, S., and Riedl, T. (2020). Impermeable Charge Transport Layers Enable Aqueous Processing on Top of Perovskite Solar Cells. Adv. Energy Mater. *10*, 1903897. https://doi.org/10.1002/aenm.201903897.

41. Dong, C., Yan, S., Liu, D., Zhu, Y., Chen, C., and Tang, J. (2025). Principle and Progress of Interconnection Layers in Monolithic Perovskite-Based Tandem Photovoltaics. Adv. Energy Mater. *15*, 2404628. https://doi.org/10.1002/aenm.202404628.

42. Jiao, Y., Wu, M., Tan, H., Wu, Y., Wu, S., Yang, Y., Liu, C., Ding, R., Cao, Y., and Mai, Y. (2025). Tailoring the C60/SnOx Bilayer to Enhance p-i-n Carbon-Electrode Perovskite Photovoltaic Cells and Modules. ACS Appl. Mater. Interfaces *17*, 35533–35540. https://doi.org/10.1021/acsami.5c05279.

43. Lukas, T., Seo, S., Holzhey, P., Stewart, K., Henderson, C., Wagner, L., Beynon, D., Watson, T.M., Kim, J.S., Kohlstädt, M., et al. (2025). Charge Extraction Multilayers Enable Positive-Intrinsic-Negative Perovskite Solar Cells with Carbon Electrodes. ACS Energy Lett. *10*, 2736–2742. https://doi.org/10.1021/acsenergylett.4c03403.

44. Chaplygin, I., Galazka, Z., Herklotz, F., and Lavrov, E.V. (2024). Ohmic contacts on SnO2 produced by hydrogen plasma treatment. Appl. Phys. Lett. *125*, 042101. https://doi.org/10.1063/5.0205615.

45. Courtright, B.A.E., and Jenekhe, S.A. (2015). Polyethylenimine Interfacial Layers in Inverted Organic Photovoltaic Devices: Effects of Ethoxylation and Molecular Weight on Efficiency and Temporal Stability. ACS Appl. Mater. Interfaces *7*, 26167–26175. https://doi.org/10.1021/acsami.5b08147.

46. Zhang, C., Son, Y., Kim, H., Lee, S.H., Liang, X., Fu, G., Lee, S.U., Park, D.A., Jiang, Q., Zhu, K., et al. (2024). Work function tuning of a weak adhesion homojunction for stable perovskite solar cells. Joule *8*, 1394–1411. https://doi.org/10.1016/j.joule.2024.02.015.

47. Musselman, K.P., Uzoma, C.F., and Miller, M.S. (2016). Nanomanufacturing: High-Throughput, Cost-Effective Deposition of Atomic Scale Thin Films via Atmospheric Pressure Spatial Atomic Layer Deposition. Chem. Mater. *28*, 8443–8452. https://doi.org/10.1021/acs.chemmater.6b03077.